Nanoscale Mixed Ion-Electron Conducting NASICON-type Thin-Films: Lithium Titanium Phosphate via Atomic Layer Deposition

Daniela R. Fontecha*[1], Alexander C. Kozen[3], David M. Stewart[1], Alex T. Hall[1], John Cumings[1], Gary W. Rubloff[1,2], Keith E. Gregorczyk*[1]

[1]Department of Materials Science and Engineering, University of Maryland, College Park, Maryland 20742
[2]Insititute for Systems Research, University of Maryland, College Park, Maryland 20742
[3]Department of Physics, University of Vermont, Burlington, VT, 05405

Abstract

Advancements in ionic devices for energy applications (e.g., solid-state micro-batteries, ionic capacitors, ion-tunable transistors, etc.) require significant development of compatible materials and fabrication processes to enable high performance conduction and storage of ions. Atomic layer deposition (ALD) enables fabrication of solid-state devices with high energy and power densities due to the complex structures made possible by its angstrom-scale thickness control and high conformality. The ionic conductivity of thin film materials fabricated by ALD has been limited by materials development and crystallinity control challenges, as suitable materials must be fabricated with both the appropriate composition and crystal structure. A mixed metal phosphate like $LiTi_2(PO_4)_3$ (LTP) is a prime candidate to push the boundary of ALD ionic materials due to the fast Li^+-conducting NASICON-type crystalline phase.

We developed a mixed ion-electron conducting NASICON-type thin film ALD process for $LiTi_2(PO_4)_3$ suitable for microbattery and pseudocapacitor applications. Compositional tunability was achieved by alternating between constituent lithium oxide (Li_2O) and titanium phosphate (TiPO) sub-processes. By adjusting the ratio between Li_2O and TiPO cycles, the Li content in LTP can be tuned between 8-34 atomic % Li. A NASICON-type crystalline structure is observed after post-deposition annealing the LTP films between 650 °C and 850 °C. The semicrystalline LTP thin film has an ionic conductivity of 9.3×10^{-7} S/cm at RT and 1.7×10^{-5} S/cm at 80 °C and an electronic conductivity of 2.5×10^{-7} S/cm at RT. In this work, we discuss the complexities of how tuning the composition of LTP influences film properties such as structure and conductivity in the mixed metal phosphate phase space.

Introduction

Atomic layer deposition (ALD) of Li^+ ion storing and conducting films is playing an increasingly important role in the manufacturing of high-performance Li^+ ion batteries (LIBs).[1–5] Application in the battery space was paved by George et al. who demonstrated cathode and anode particle coating to functionalize or passivate the surface.[4,6,7] This advancement led to commercialization of thin film-stabilized anode and cathode composites in LIBs.[8–10] Since, thin-films of Al_2O_3, $LiNbO_x$, etc. have been used to control interfacial degradation, inter-particle contact, and reduce dendrite growth in advanced LCO-based (i.e. NCA, NMC, etc.) electrodes.[11–13] Additionally, these materials and processes are beginning to have applications beyond next generation solid-state microbatteries (SSMBs) including;[14] solid-state Li^+ ion supercapacitors,[15] and other advanced iontronic devices where ions contribute as a signal carrier (i.e. ion-tunable transistors,[16] ionic memristors,[17] electrochromics,[18] etc.). Solid-state systems have several advantages including increased device density, flexible device footprint, and increased power and energy density enabled by the conformality and angstrom-scale control achievable by ALD.

Thin film electrodes tend to have higher rate capabilities thanks to short transport length at the scale of 10's of nanometers. However, this can be further improved by utilizing materials with high Li^+ ion mobilities.[19] Despite this interest, the Li^+ ion conductivity of ALD thin films remains less than 10^{-6} S/cm, limiting the both application and performance in iontronic devices. Several electrode materials have been developed by ALD with $LiCoO_2$, $Li_{1+x}Mn_{2-x}O_4$, $LiFePO_4$, etc., as cathodes[20–23] and SnO_2, SnO_xN_y, TiN,

V_2O_5, TiO_2, Nb_2O_5, $Li_4Ti_5O_{12}$ etc., as anodes.[15,24–28] However, there have yet to be ALD electrodes that take advantage of high Li^+ mobility phases such as the NASICON-type crystalline phase of $LiTi_2(PO_4)_3$ (LTP).

A mixed metal phosphate like LTP is a prime candidate with a Li^+ ion conductivity on the order of 10^{-6} to 10^{-5} S/cm due to its NASICON-type crystalline phase. This crystalline phase allows for fast Li^+ ion conduction through a 3D network in interstitial sites between TiO_6 octahedra and PO_4 tetrahedra.[29–31] Slight doping of LTP (e.g. Al^{+3}, Cr^{+3}, Ga^{+3}, Sc^{+3}, Y^{+3}, In^{+3}, or La^{+3}) can generate several orders of magnitude improvements in ionic conductivity up to 10^{-3} S/cm by altering the unit cell parameters and densifying the film microstructure.[32–36]

LTP is traditionally an electron-blocking material, but it has been successfully made into an anode by mixing it with an electron-conducting material such as carbon or TiO_2 such that there exists a continuous electron conduction pathway.[37–40] Crystalline LTP has been demonstrated as an anode material for aqueous alkali-ion batteries due to its chemical stability with water, a reaction potential of -0.5 V vs SHE, and reversibility of Li^+ ion intercalation up to $Li_3Ti_2(PO_4)_3$.[37–41] As LIB anode, LTP-carbon composites were cycled reversibly in two different potential windows – $LiTi_2(PO_4)_3$ to $Li_3Ti_2(PO_4)_3$ from 1.5 to 3.5 V vs Li^+/Li and $Li_3Ti_2(PO_4)_3$ to $Li_6Ti_2(PO_4)_3$ from 0.25 to 1.2 V vs Li^+/Li.[42–45] This body of literature demonstrates LTP as a material that has the potential to be adopted into multiple components of iontronic devices.

This work reports the first instance of a NASICON-type ALD LTP thin film. We discuss the versatility of this novel LTP process and the effects of composition on structure and electrical properties. It exhibits an ionic conductivity of 9.3x10^{-7} S/cm at room temperature and 1.2x10^{-5} S/cm at 80 ^{o}C and an electronic conductivity of 2.5x10^{-7} S/cm at room temperature, making it a good candidate as a composite thin film electrode for microbatteries and pseudocapacitors.

Experimental

ALD Process Development. Test-grade wafers (University Wafer) were pumped down to 10^{-7} Torr in a load-lock chamber before transferring them into the ALD reactor. Depositions were conducted at 300 ^{o}C in a Cambridge Nanotech (now Veeco) Fiji F200 Gen 1 ALD reactor coupled to an ultra-high vacuum (UHV) cluster system (<10^{-8} Torr). ALD precursors were lithium tert-butoxide (LiO^{t}Bu) (Sigma, 97%), deionized water, trimethylphosphate (TMP) (Sigma, 99%), and titanium (IV) isopropoxide (TTIP) (Sigma, 99.99 %) with argon (Airgas UHP, 99.999%) used as the carrier gas. The base pressure of the ALD reactor was 1x10^{-6} Torr, and the process pressure was maintained at 200 mTorr by flow of UHP argon (Airgas, 99.999%) gas.

LiO^{t}Bu was kept at 150 ^{o}C in a stainless-steel bubbler and delivered to the ALD reactor with 40 sccm argon carrier gas flow. H_2O was kept at room temperature, TMP was kept at 70 ^{o}C, and TTIP was kept at 100 ^{o}C. H_2O, TMP, and TTIP were all kept in stainless-steel vapor draw cylinders. ALD films were deposited with lithium oxide and titanium phosphate subprocesses. The lithium oxide subprocess consisted of a 5 second LiO^{t}Bu pulse, and a 0.06 second H_2O pulse. The titanium phosphate subprocess consists of a 0.2 second TMP pulse followed by a 0.06 second water pulse and a 0.1 second TTIP pulse followed by a 0.06 second water pulse. All processes have 20 second Ar purge after each precursor pulse.

Real-time *in-situ* monitoring of film thickness was performed using a J.A Woollam M-2000D spectroscopic ellipsometer with a spectral range of 193-1000 nm. Film thicknesses were fit to an optical Cauchy model and the measurements then verified by cross-sectional scanning electron spectroscopy (SEM).

Sample Preparation. X-ray photoelectron spectroscopy (XPS) and X-ray diffractometry (XRD) were performed on films deposited on bare p-doped Si(100) test-grade wafers (University Wafer) with resistivity of 1-100 ohm-cm because Si does not interfere with the measurements in this case. Raman spectroscopy and electrochemical impedance spectroscopy (EIS) were performed on films deposited on Si chips with 500 nm thermal SiO_2, 10 nm Ti, and 100 nm Pt (i.e. $Si/SiO_2/Ti/Pt$ stack).

Annealing procedures. For Raman, XRD, and XPS, films were annealed at various times and temperatures in a tube furnace under a flowing N_2 environment. Some films were allowed to radiatively cool and others were quenched to room temperature on a metal table acting as a heat sink. For impedance measurements, films were annealed in the rapid thermal annealer (RTA) at 650 ^oC for 8.5 minutes under a flowing N_2 atmosphere and subsequently quenched to room temperature.

X-Ray Photoelectron Spectroscopy (XPS). Post-deposition, films were transferred under UHV to a Kratos Ultra DLD Surface Analysis system ($1x10^{-9}$ Torr) for XPS analysis. XPS data were collected using a monochromatic Al Kα (1486 eV) X-ray source at 15 kV and a total anode power of 150 W. Survey spectra were collected with a pass energy of 160 eV and binding energy step size of 1 eV. High resolution spectra were collected with a pass energy of 20 eV and a binding energy step size of 0.1 eV at the appropriate number of scans to produce a satisfactory signal/noise ratio. Casa XPS was used to analyze all data. XPS peaks were fit using a Shirley background and 30/70 Gaussian/Lorentzian pseudo-Voigt functions. Elemental quantification was done by comparing the ratios of high-resolution peak areas with the tabulated Kratos relative sensitivity factors. All spectra were charge calibrated to the C 1s peak at 284.8 eV.

X-Ray Diffraction (XRD). XRD was performed by a PANalytical XPert Pro MRD system in a grazing-incidence (GI)-XRD configuration with a scan rate of 0.025 ^{o}/s and step size of 0.05 ^{o}. Cu-Kα (λ = 1.54 Å) radiation source was used. The diffraction patterns were compared with primary references from the International Center for Diffraction Data (ICDD) for identification. Rietveld Refinement was performed using Profex.

Raman Spectroscopy. Measurements were recorded in air with a "Labram HR" microscope system (Horiba Jobin Yvon USA). A 633 nm laser (HeNe) with a D1 intensity filter was used. The incident laser power was controlled to 1 mW and ~2µm diameter spot size with a 100x microscope objective. A 600 gr/mm grating was used for acquisitions with 20s exposure and 5 repetitions.

Microscopy. Scanning electron microscopy (SEM) and focused ion beam (FIB) cross-sections were performed on a dual-beam field emission SEM/FIB system (Tescan, XEIA3) with a 10 kV acceleration voltage. Transmission electron microscopy (TEM) imaging was performed using a JEOL JEM-2100F operated at 200 kV. All images were formed on a Gatan OneView CMOS camera. ***Sample preparation:*** TEM cross-sections were prepared by hand polishing using a PELCO Tripod Polisher followed by final thinning in a Gatan PIPS II ion polisher.

Impedance Measurements. Electrochemical impedance spectroscopy (EIS) was performed with a Biologic VSP potentiostat in an argon-filled glovebox (MBraun) maintained at <0.5 ppm H_2O and O_2. Finished devices were placed on a custom-built mica glass-ceramic stage with a proportional integral-derivative (PID) temperature controller. Electrical contact was made with micromanipulator probes. EIS measurements were made at temperatures between 25 and 100 ^oC at frequencies of 200 kHz to 250 mHz with an AC amplitude of 20 mV. DC relaxation was performed by applying a series of DC voltages (50, 100, 350, 500 mV) for 10 minutes each. *Sample Preparation:* LTP was deposited on $Si/SiO_2/Ti/Pt$ stacks. The Pt layer serves as the bottom contact for the metal-insulator-metal stacks. Once LTP is deposited, the chips were annealed in the rapid thermal annealer (RTA) at 650 ^oC for 8.5 minutes under a flowing N_2 atmosphere. Post-anneal, a stainless-steel shadow mask with circular holes 400 um in diameter was placed above the LTP layer to pattern a top current collector of Au, forming a vertical Pt/LTP/Au stack for impedance testing. A 120 nm Au top-contact was deposited on the samples without air-exposure using a resistive metal evaporator integrated with the UHV cluster system.

LTP Process Development

Super-cycling is a common method for controlling film composition by alternating between binary ALD cycles in different thickness ratios.[22,24,46,47] ALD sub-processes of lithium oxide (Li_2O) and titanium phosphate (TiPO) were used to modulate the stoichiometry of LTP as shown in ***scheme 1a***. Adjustment of the LTP stoichiometry was achieved by indexing the super-cycling ratio, *n*, between the values of 1-10. ***Scheme 1b*** shows an exaggerated representation of the film growth with this super-cycling approach. The TiPO composition can be quite adaptable depending on the precursor choice, reaction temperature, and post-annealing conditions.[48–54] For LTP to function as an anode, it requires a source of electronic conductivity which can be achieved with intermixed TiO_2 grains.[55] In this work, a thermal TiPO process with TMP, TTIP, and H_2O precursors was chosen as described in the experimental section to simultaneously introduce a phosphate and oxide component, similar to previous works.[48,50,52]

The atomic composition with respect to the super-cycling ratio is shown in **Figure 1a** in which a ratio of $n = 0$ is titanium phosphate only. Quantitative analysis of the titanium phosphate film approximately indicates a 1:2 ratio of TiP_2O_7:TiO_2. The lithium atomic % varies the most across the super-cycling range (34.4 to 8.3 atomic %). The titanium atomic % increases gradually with increasing super-cycling ratio until it stabilizes at 14.5 atomic % for ratios greater than six – indicating an upper limit of tunability of the LTP process. The oxygen atomic % ranges most drastically between super-cycling ratios of 1 to 2 by 13.2 atomic %, after which the oxygen content stabilizes at ~55-58 atomic %. This is likely due to the sudden decrease in oxygen rich pyrophosphate (TiP_2O_7) at the super-cycle ratio of 1 compared to the higher super-cycle ratios.

Scheme 1. Super-cycle method for LTP process development.

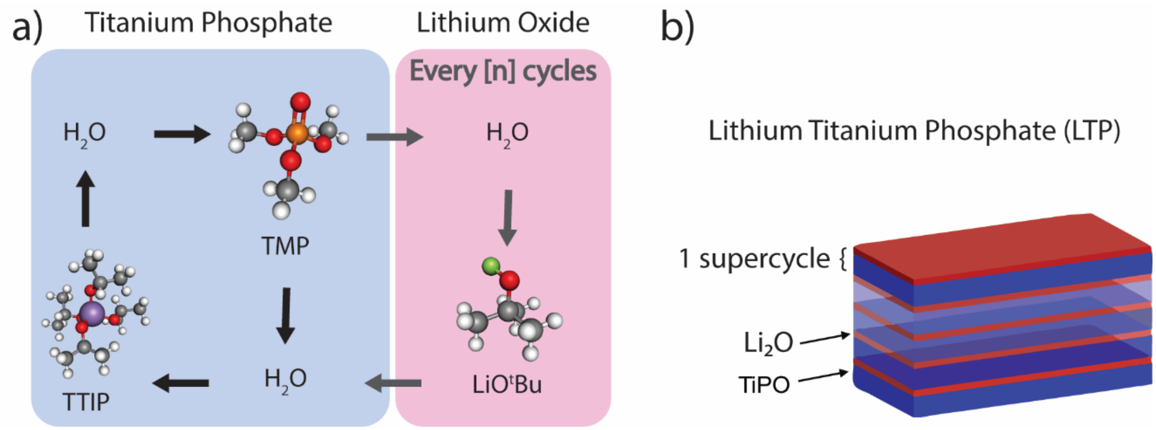

a) Super-cycle process diagram for LTP with lithium *tert*-butoxide (LiOtBu), trimethyl phosphate (TMP), titanium tetraisopropoxide (TTIP) and water. b) Thin film representation of sub-cycles of Li_2O and TiPO to form one super-cycle.

Figure 1b-f shows high resolution XPS spectra for the as-deposited TiPO and LTP films deposited at 300 °C as well as post-annealed at 850 °C for 3 hours. For the as-deposited TiPO film, the Ti 2p peak exhibits spin orbit splitting (j = ½ at 465.1 eV and j = 3/2 at 459.4 eV) and a chemical shift that suggests that Ti is in the +4 oxidation state.[48,54] The P 2p spectra exhibits spin orbit splitting with the j = 3/2 at 133.6 eV and j = ½ at 134.5 eV. The TiPO O 1s spectra has 3 components at 530.1 eV, 531.2 eV, and 533.0 eV corresponding to Ti-O, P-O-P, and a minor component of C-O bonding, respectively.[48,52,54,56] This agrees with the compositional analysis of the as deposited TiPO film containing a mixture of TiO_2 and TiP_2O_7.

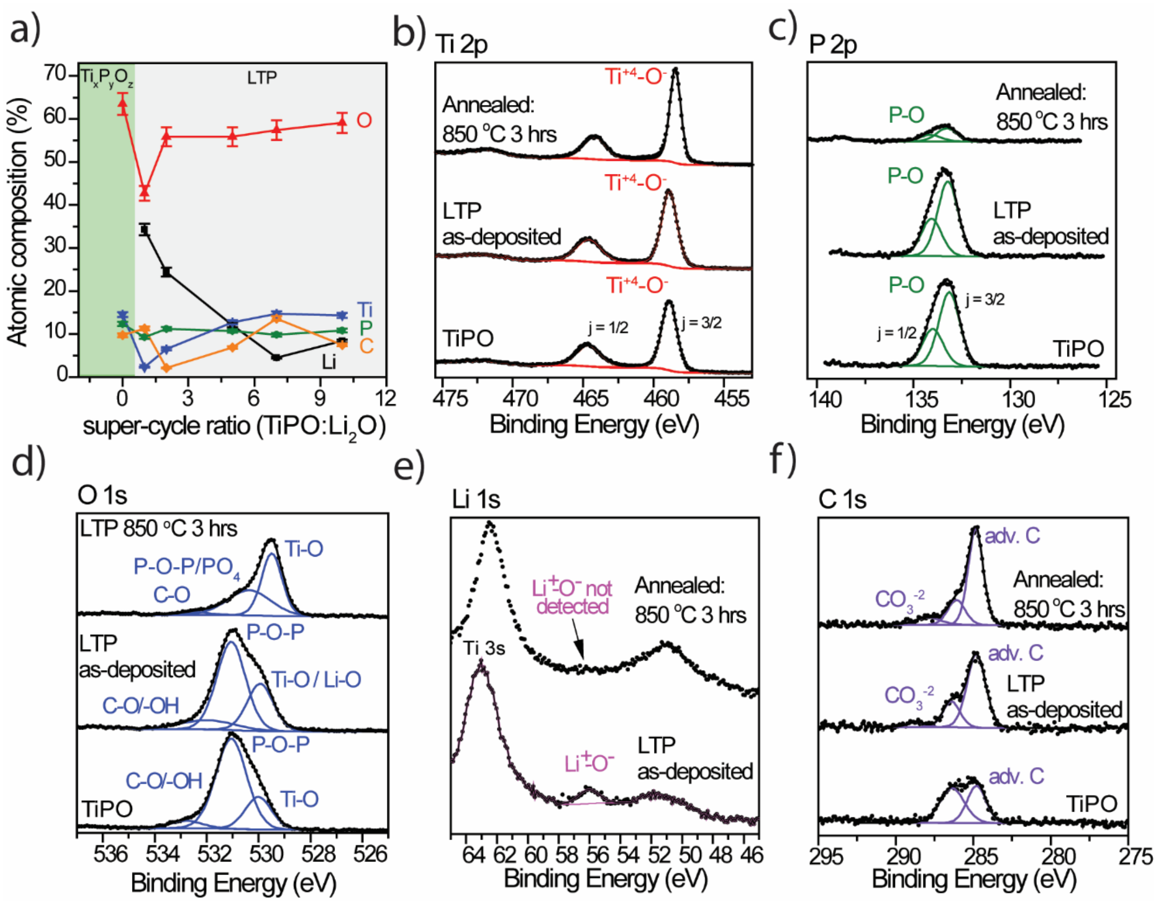

Figure 1. a) Atomic composition of LTP system with respect to super-cycle ratio. High resolution XPS spectra of b) Ti 2p, c) P 2p, d) O 1s, e) Li 1s and f) C 1s for TiPO, LTP (n= 7) as deposited, and LTP (n = 7) annealed at 850 °C for 3hrs.

XPS of the as-deposited LTP film detects 4.5 atomic % lithium with a binding energy of 56.0 eV. The O 1s, Ti 2p, and P 2p spectra in LTP remain largely unchanged upon addition of Li by the super cycling method. However, the C-O component in the O 1s region of as-deposited LTP appears broader and is shifted to lower binding energies by 0.5 eV compared to TiPO. This is likely due to formation of Li-OH from the Li_2O monolayers which overlaps with the low end of the C-O binding energy region.[57] Additionally, the peak previously assigned at Ti-O is slightly broader and more intense due to the presence of Li-O bonds that overlap with this region.[48,52,57]

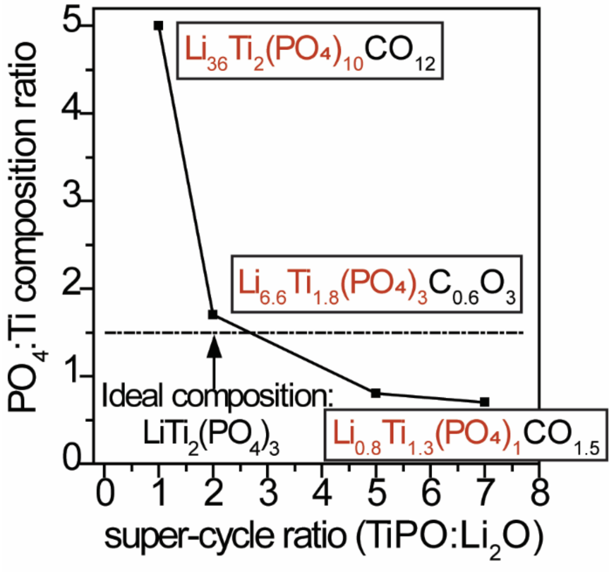

Figure 2. Ratio of PO_4:Ti with respect to super-cycle ratio as an ideality marker of the LTP stoichiometry.

There is a large collection of literature on bulk LTP that indicates the ideal composition is $LiTi_2(PO_4)_3$ for optimized ionic conductivity of this material in its NASICON-type crystalline phase due to the Li^+-conducting 3D network that is formed.[31,36,58] In **Figure 2** we show the stoichiometries at each super cycle ratio along with the ideal ratio defined as PO_4:Ti (a ratio of 1.5 corresponds to the ideal LTP stoichiometry). The PO_4:Ti ratio has a decaying profile with increasing super-cycling ratio. At one extreme (super-cycle ratio, n = 1) there is excess of both Li and PO_4 in the film, with a composition of $\mathbf{Li_{36}Ti_2(PO_4)_{10}}CO_{12}$. On the other extreme (super cycle ratio, n = 7), there is excess Ti with a composition of $\mathbf{Li_{0.8}Ti_{1.3}(PO_4)_1}CO_{1.5}$. The middle ground appears to be with a super cycle ratio of 2 where there is good agreement between the ideality ratio while also retaining some excess Li in the film (with a composition of $\mathbf{Li_{6.6}Ti_{1.8}(PO_4)_3}C_{0.6}O_3$) before annealing.

Figure 2 summarizes these data and demonstrates the chemical tunability of the process, in which the super cycle ratio can be chosen such that there is excess Li, PO_4, or

Ti in the as-deposited film. We primarily focus on LTP films with super cycle ratios of 1, 2, and 7 to illustrate the consequences of starting film stoichiometry on post-annealing crystal structure and electrochemical performance in the NASICON-type family of materials.

Structural Characterization

Starting with the composition of a super cycle ratio of n = 7, **Figure 2** shows a Li and PO_4-deficient film relative to the predicted stoichiometry of the NASICON-type LTP phase (straight-line PO_4:Ti = 1.5). **Figure 3a** shows the Raman spectrum of this film annealed at 850 ^{o}C for 10 hrs that was allowed to cool radiatively over the course of 10 hours. This complex Raman spectrum can be deconvoluted into a variety of phases: TiO_2 anatase, TiO_2 rutile, TiO_2 brookite, $LiTiPO_5$, γ-Li_3PO_4, β-Li_3PO_4, $TiPO_4$, and TiP_2O_7, with the peak assignments summarized in ***Table 1***.[59–66] Although the characteristic NASICON-type peaks are not present here, TiO_2 and $LiTiPO_5$ are common impurities in bulk NASICON-type LTP and LATP found in literature.[67] The complexity of this film is owed to the extended time at elevated temperatures, which we hypothesize enables constant rearrangement of atoms that crystallize into various types of phosphates and oxides depending on the local composition. Therefore, control over the film structure can be achieved by annealing for shorter times and quenching to room temperature at the end of the annealing period.[68]

Table 1. Raman peak assignments for representative LTP n = 7, 2, and 1 annealed films. A more complete table list all of the samples discussed in the manuscript can be found in the SI (**SI-2**).

Phase	ref. wavenumber	ref.	LTP (n = 7) 850C		LTP (n = 2) 650 oC	LTP (n =1) 850C
			10 hrs	3 hrs	1 hr	30 min center
TiO_2 anatase	147	[59]	147			
	198			195	198	193
	398			395	396	393
	515			515	518	516
	640			636	637	637
TiO_2 rutile	144	[59]		142	143	142
	235		233			
TiO_2 brookite	153	[60]	151			
	214		213			
$LiTiPO_5$	745	[64]	749			
NASICON	214	[61]	213			
	239			237	238	238
	273			272	278	271
	309			308	310	309
	351			348	350	347
	432			431	430	431
	446			444	446	445
	970			967	967	966
	989			985	986	986
	1006			1003	1004	1003
	1017		1011			
	1095			1092	1095	
$TiPO_4$	173	[65]		172		
	294		290			
	606		604			
	1047		1051			
β-Li_3PO_4	478	[62	475			
	478		481			
	586		583			
	622		625			
	1023		1022			
	1023		1027			
	1063		1063			
γ-Li_3PO_4	426	[62]	421			
	607		604			
	631		625			
	1023		1022			
	1023		1027			
	1063		1063			
TiP_2O_7	625	[63]	625			

To address this, we annealed the n = 7 sample for 3 hrs and introduced a post anneal quench to room temperature. The resulting Raman spectrum (**Figure 3a**) has characteristic NASICON-type peaks in the high wavenumber region (965 – 1095 cm^{-1}) and in the lower wavenumber region (237 – 445 cm^{-1}), matching the NASICON-type LTP reference peaks detailed in ***Table 1***. The remaining peaks match TiO_2 anatase and rutile. This is a significant improvement in the phase purity of the film, owed to shorter exposure to high temperatures. As discussed in the previous section, the base TiPO ALD process already contains a TiO_2 phase impurity from the TTIP/H_2O step.[52,69] Having pre-formed amorphous TiO_2 can lead to preferential anatase grain growth, which is observed in both annealing conditions discussed here.

The XPS spectra of the n = 7 film annealed at 850 °C for 3 hrs reveals a drastic loss of P (from 9.8 to 3.4 atomic %) and Li (from 4.5 to 0 atomic %) paired with an increase in C content (from 13.6 to 24.9 atomic %) on the surface (**Figure 1b-f**). Before annealing, the C 1s spectra of as-deposited LTP has a peak at 288.8 eV, which lies in between lithium carbonate and titanium carbonate reported peak positions.[52,70] After the 850 °C anneal in air, the C 1s spectra for LTP has a peak at 287.6 eV that corresponds to carbonyl groups (C=O). Since there is also no more Li present in the LTP sample after the anneal, this suggests that most of the carbonates from the as-deposited LTP were Li_2CO_3 and were converted into organic carbonyl groups as the Li evaporated from the film.[71] The O 1s peaks of the annealed LTP more closely match semi-crystalline Li_3PO_4,[72,73] with a phosphorous component peak shift to lower binding energies at 530.5 eV, suggesting a change in structure at high temperatures formed PO_4 tetrahedral units. The Ti 2p in the annealed LTP shows a shift to lower binding energies by 0.3 eV, indicating a change in chemical environment attributable to TiO_6 octahedra formation.[74]

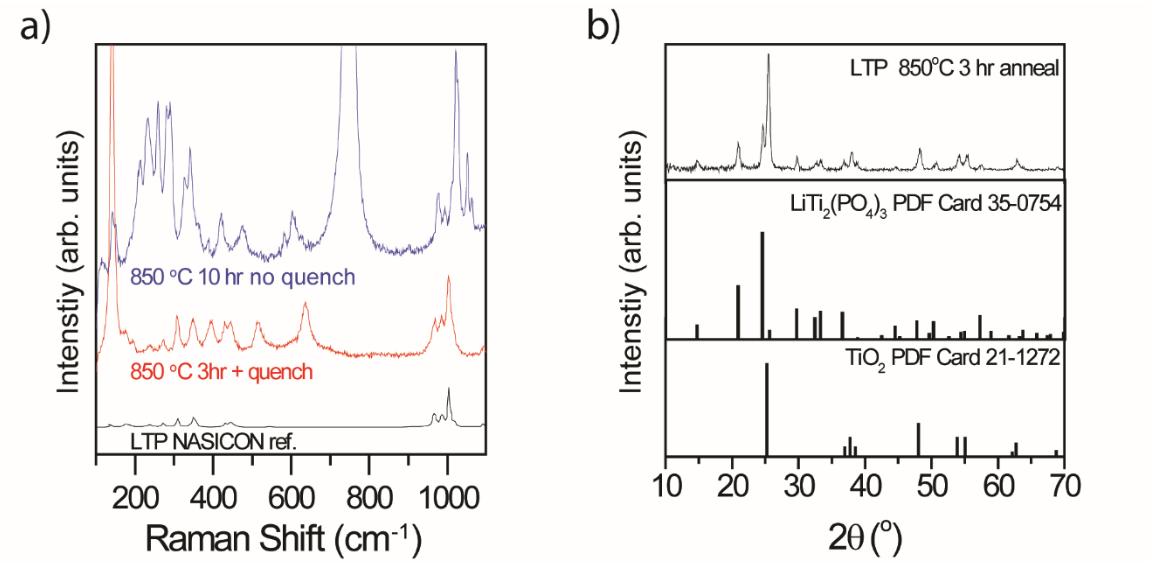

Figure 3. a) Raman spectra for LTP (n = 7) annealed at 850 °C for 10 hrs (blue) and 850 °C for 3 hrs and quenched (red). b) GI-XRD of LTP (n = 7) annealed at 850 °C for 3 hrs and quenched (top) with reference spectra of NASICON-type LTP (middle) and TiO_2 anatase (bottom).

Crystallographic characterization was performed with GI-XRD of the n = 7, Li and PO_4-deficient LTP film annealed at 850 °C for 3 hrs as shown in **Figure 3b**. There is a match between the annealed LTP sample and characteristic NASICON-type LTP crystalline peaks, particularly at 14.8 °, 20.9 °, 24.5 °, 29.8 °, 32.5 °, and 33.4 ° 2(θ). Although the (101) face of TiO_2 anatase overlaps with the (113) face of NASICON-type LTP,[75] TiO_2 anatase can be identified by three characteristic peaks at 36.9 °, 37.9 °, and 38.6 ° 2(θ).[76] Rietveld refinement of the LTP GI-XRD spectra estimates a relative composition of 55.2 % anatase TiO_2 and 44.8 % NASICON-type LTP (**SI-4**).

Although the NASICON-type phase is observed with improved annealing conditions, **Figure 4** demonstrates that phase inhomogeneities exist spatially across the LTP films for Li and PO_4-deficient samples. **Figure 4a** shows the two extreme compositions (n = 7 and n = 1) annealed at 850 °C for 30 minutes with Raman spectra taken at the center and edge of the samples. Li and PO_4-rich films (n =1) show good uniformity with nearly identical spectra at the center and edge. However, in the Li and PO_4-deficient films, there is a spatial phase non-uniformity present. The center contains $LiTiPO_5$, TiO_2 anatase, and $TiPO_4$. There are additional peaks in the high wavenumber region (966-1050 cm^{-1}) that are likely overlapping mixed phosphate peaks and difficult to identify. However, the edge has crystalline phase contributions of NASICON-type LTP, TiO_2 anatase and TiO_2 rutile only. This disparity is likely due to compositional gradients which appear to become homogeneous given enough excess Li and P in the initial film composition to compensate for Li loss at high temperatures.

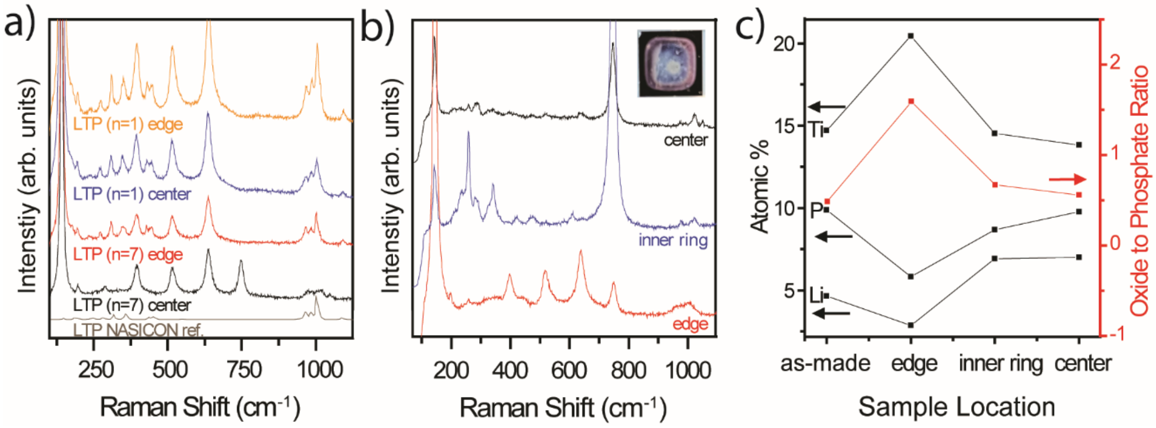

Figure 4. a) Raman spectra of Li and PO_4-deficient (n = 7) films annealed at 850 °C for 30 min taken at the center (black) and edge (red) compared to Li and PO_4-rich films taken at the center (blue) and edge (orange). b) Raman spectra of Li and PO_4-deficient (n = 7) films annealed at 650 °C for 10 hrs without quenching taken at the edge (red), inner ring (blue), and center (black). c) XPS compositional analysis of the Li, Ti, and P concentrations (left axis) and the TiO_2:PO_4 ratio from the O 1s high resolution spectra corresponding to the same regions as (b).

To verify the existence of a compositional gradient, XPS and Raman mapping were performed on Li and PO_4-deficient (n = 7) samples that were annealed at 650 °C for 10 hrs without quenching (**Figure 4b**). The inset in **Figure 4b** of the annealed sample shows an obvious inhomogeneity within the sample with three distinct regions: the center white dot, the blue inner ring, and the purple edge. Raman and XPS spectra were taken at each of these regions. The Raman spectra (**Figure 4b**) show phase non-uniformity in which the edge of the sample contains NASICON-type LTP, $LiTiPO_5$, and TiO_2 phases while the inner ring and center show dominant $LiTiPO_5$ peaks, with lower intensity TiO_2 anatase, brookite, rutile, $TiPO_4$, γ-Li_3PO_4, and β-Li_3PO_4. The XPS map (**Figure 4c**) taken in the same regions displays a Li and P gradient increasing from the edge to the center while the Ti decreases in the same direction. The ratio of oxide to phosphate in the O 1s high resolution spectra (**SI-5**) was quantified to compare to the phases observed in the Raman map. The edge of the sample has the most intense TiO_2 Raman peaks accompanied by NAISON peaks (**Figure 4b**). In **Figure 4c**, the TiO_2:PO_4 ratio decreases quickly from the edge (1.6) to the inner ring (0.7) where it stabilizes compared to the center (0.6). In the Li and P-rich regions the $LiTiPO_5$ phase appears dominant. Since this anneal ramps down slowly without quenching, and $LiTiPO_5$ crystallizes at 570 ^{o}C (~280 - 90 ^{o}C lower than NASICON-type LTP),[77] it is likely that the $LiTiPO_5$ phase is more readily available at lower temperatures, leaving little to no Li and P to form the NASICON-type phase in the center and inner ring. The annealing condition in **Figure 4b** follows the same pattern as the Raman spectra of the 850 ^{o}C 30 min quenched anneal in **Figure 4a**, in which $LiTiPO_5$ and $TiPO_4$ consume Ti at the expense of TiO_2. In instances where the dominant phosphate phase is NASICON-type, little to no other phosphates are observed, leading to abundant resources for TiO_2 formation.

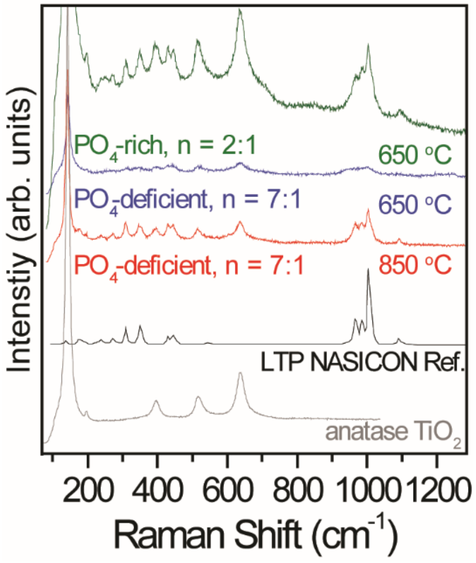

Figure 5. Raman spectra of Li and PO$_4$-rich (n = 2) and Li and PO$_4$-deficient LTP (n = 7) annealed at 650 °C and 850 °C for 1 hour under N$_2$ flow.

In addition to phase homogeneity, initial composition has an effect on the temperature required to observe the NASICON-type phase. In **Figure 5,** Raman spectra of Li and PO$_4$-deficient films are compared to Li and PO$_4$-rich films. Peaks associated with anatase TiO$_2$ anatase and TiO$_2$ rutile are present in all cases (See SI for tabulated values in **SI-2**). The characteristic NASICON-type peaks are very prominent in the 850 °C annealed condition of the Li and PO$_4$-deficient film (n = 7). This signature is diminished when annealed at 650 °C for the same amount of time. In contrast, at an annealing temperature of only 650 °C the Li and PO$_4$-rich film (n = 2) shows well-defined NASICON-type peaks in the high wave number region with relatively high intensities. Typical synthetic methods for LTP in the bulk require high temperature processes (ranging from 800 – 1450 °C) to achieve the desired structure.[36] A reduction in crystallization temperature as much as 200 °C is achieved by starting with a Li and PO$_4$-rich LTP film. In this case 650 °C is required –

a much lower annealing requirement than in bulk NASICON-type SSEs. Reduced thermal budgets is a feature of thin films that can be leveraged with ALD given the angstrom-scale thickness control it affords.

The structure of the Li and PO_4-rich films (n = 2) are studied in greater detail to elucidate a physical representation of the phase distribution that will aid in our impedance analysis in the next section. The n = 2 samples were annealed in a rapid thermal annealer (RTA) at 650 ^oC for 9 min (Raman shown in **SI-1b** and GI-XRD shown in **SI-6**). These conditions were chosen with a metal-insulator-metal (MIM) stack in mind to minimize the well-documented volume shrinking known to occur in LTP upon crystallization, such that the film remains continuous after the annealing step.[68,78] SEM cross-sectional images in **SI-9** show the morphological improvement on the annealed LTP film from 850 ^oC for 3 hrs to 650 ^oC for 9 min suitable for an MIM stack. Raman and GI-XRD of this material indicates that it is a semicrystalline film with a mixture of anatase TiO_2 and NASICON-type LTP grains with an average size of 29.0 nm and 44.1 nm, respectively (Scherrer analysis included in **SI-3**). High-resolution transmission electron microscopy (HRTEM) confirmed a large variation in particle size, with particles of both anatase TiO_2 and NASICON-type LTP ranging from ~ 5 – 40 nm in an amorphous matrix. No individual particles with sizes near the film thickness were observed. Particles were identified as anatase TiO_2 or NASICON-type LTP by comparing d-spacings observed in XRD to those observed in HRTEM and selected area electron diffraction (SAED). **Figure 6a-b** shows representative HRTEM and corresponding SAED patterns for isolated NASICON-type LTP and TiO_2 particles.

The HRTEM cross section of the LTP film in **Figure 6c** shows contrast from both crystalline and amorphous regions. The LTP and TiO_2 particles appear to be uniformly distributed in an amorphous matrix in the film. Based on their estimated weight percentage and particle size, it is plausible for there to be a continuous pathway of TiO_2 grains throughout the 60 nm thickness of the film. A schematic of the system for the Li and PO_4-rich (n = 2) film is proposed in **Figure 6d** based on the evidence shown in **Figures 1, 3, and 6**. Due to the complexity of the system created by annealing a 5-component ALD film, a specific composition cannot be assigned to the amorphous region. This physical representation of the system is used in the following section to develop an equivalent circuit model for the EIS results.[79]

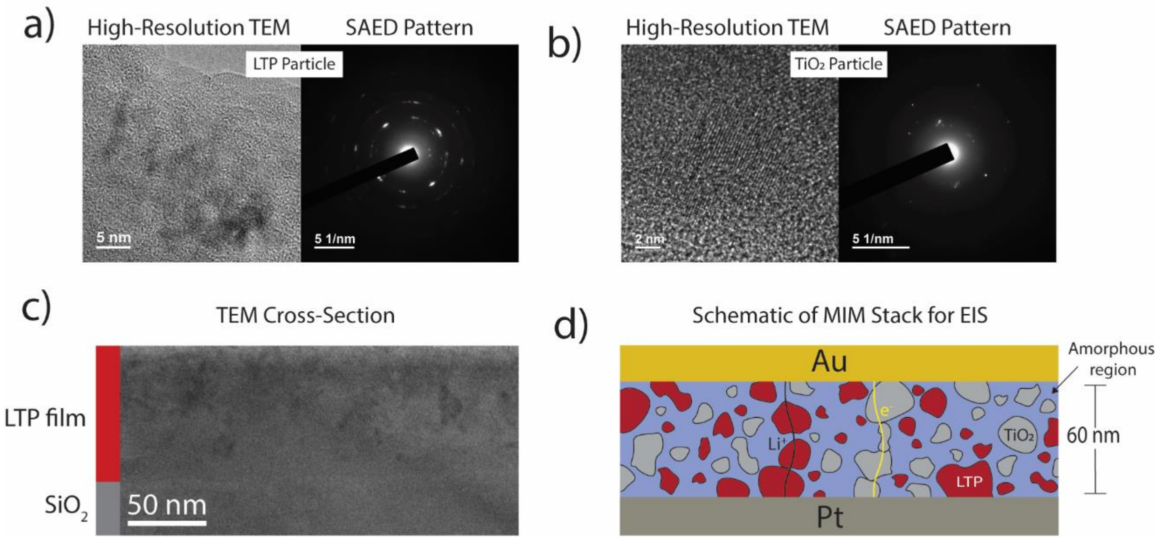

Figure 6. Annealed LTP (n = 2) (650 °C for 9 min) cross section. High-resolution TEM and corresponding SAED pattern for a) an LTP particle and b) a TiO_2 particle. c) TEM cross-section of the annealed LTP. d) Schematic cross-section of the annealed LTP film in an MIM stack configuration based on TEM and crystallographic evidence.

Impedance Analysis

The Li and PO_4-rich (n = 2) LTP thin films from **Figure 6** were studied electrochemically in a MIM stack of Pt/LTP/Au due to the low crystallization temperature required to observe the desired phases. Based on the Schematic in **Figure 6d**, we must consider the effects of the high percentage of TiO_2 on the electronic properties of this film. TiO_2 is a mixed conductor with an electronic conductivity ranging from 10^{-7}-10^{-5} S/cm[80] and has been known to serve as an anode material in LIBs.[81] Due to the significant TiO_2 impurity present upon annealing, we expect there to be both an electronic leakage pathway through the TiO_2 grains and a Li^+ ion conduction pathway through the LTP grains. Both possible conduction pathways exist in parallel in this semicrystalline film (depicted in **Figure 6d**) and must be considered in the impedance analysis. The LTP bulk and amorphous components of the film will be constructed in series to represent the Li^+ ion conduction path in the semicrystalline film (depicted in **Figure 6d**).

The mobile species are represented in the equivalent circuit model in **Figure 7a** (based on the schematic in **Figure 6d**) which was used to fit the Nyquist plots. In this equivalent circuit model, constant phase elements (CPEs) are used to represent imperfect capacitances in the material. CPE_{gb}, $CPE_{interface}$, and CPE_{bulk} represent capacities at the grain boundaries, the film/metal interface, and the bulk of the film, respectively. R_{TiO2} represents the electronic conduction through TiO_2 grains. R_{LTP} and R_{gb} represent Li^+ ion conduction through the LTP grains and the grain boundaries, respectively.

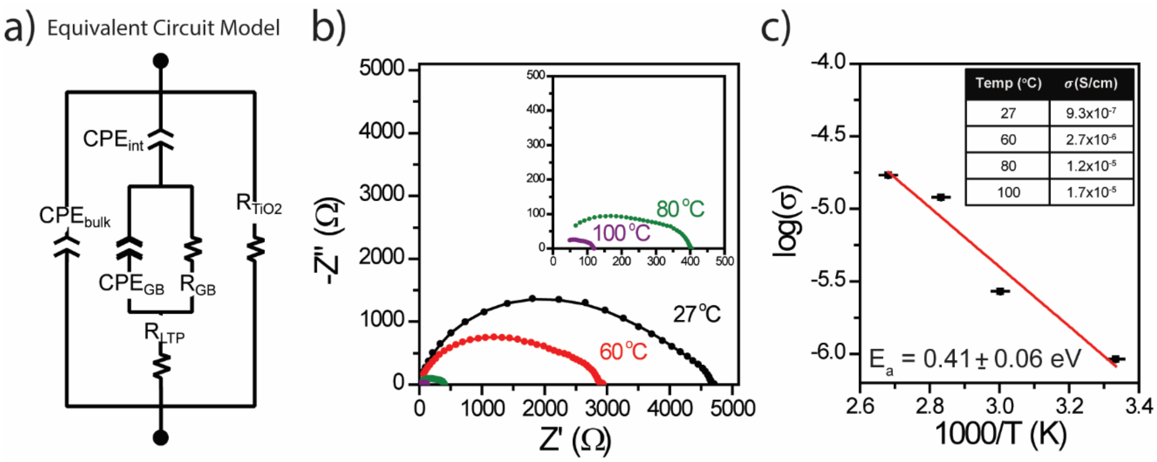

Temp (°C)	σ (S/cm)
27	$9.3x10^{-7}$
60	$2.7x10^{-6}$
80	$1.2x10^{-5}$
100	$1.7x10^{-5}$

Figure 7. Electrochemical data for LTP (n = 2) in MIM stack annealed at 650 °C for 9 min in the RTA. a) The equivalent circuit model used to fit the EIS data for the Au/LTP/Pt stack. b) Nyquist plots of Au/LTP/Pt probed at 27, 60, 80, and 100 °C. c) Arrhenius plot of LTP with the respective ionic conductivities at each temperature.

The room temperature Nyquist plot in **Figure 7b** shows an asymmetric semicircle that approaches the real axis at the low frequency limit. This indicates an electronic leakage pathway consistent with the density of TiO_2 impurities measured by GI-XRD, Raman spectroscopy, and HRTEM. The equivalent circuit model fitting results in a TiO_2 electronic conductivity of $2.5x10^{-7}$ S/cm, in agreement with the total film electronic conductivity measured by DC relaxation experiments (shown in **SI-7**).

This result, in conjunction with the TiO_2 peak positions in the Raman and XRD in **Figure 3** indicate, that the anatase TiO_2 present in the film is not lithiated after annealing.[64,76] Q. Zhang et al., have demonstrated LTP as an anode material for aqueous LIBs by a hydrothermal synthesis method in which TiO_2 anatase nanoparticles formed a 3D interconnected network that allowed electronic conduction through the film.[38] In a similar fashion, the EIS in **Figure 7b** shows that this LTP film has a high enough TiO_2 phase fraction to be a candidate as an anode material as reported.

The corresponding LTP bulk and grain boundary Li^+ ion conductivities of this film are 9.3 x 10^{-7} S/cm and 5.6 x 10^{-9} S/cm, respectively at room temperature. The total ionic conductivity of LTP can range between 10^{-8} to 10^{-6} S/cm due to the grain boundary composition and overall porosity of LTP.[36,82] Determining the composition of the amorphous region is difficult, but it is likely some form of glassy lithium phosphate intermixed with carbon which can have ionic conductivities on the order of 10^{-9}'s to 10^{-8}'s S/cm.[72,83]

The sample temperature was adjusted *in situ* to produce the rest of the EIS data shown in the Nyquist traces in **Figure 7b** and the Arrhenius plot in **Figure 7c**. The Nyquist plots show a reduction in overall impedance of the film at elevated temperatures, as well as a slight change in the ratio between the two semi-circle elements in the impedance. The latter implies two different activation energies for the transport they represent (see **SI-8**). The Arrhenius plot shows a linear relationship between the log of ionic conductivity calculated from R_{LTP} and temperature – indicating an ion hopping mechanism in the LTP grains.[84] The LTP bulk has an activation energy of 0.41 ± 0.06 eV, which closely matches literature for a semicrystalline NASICON-type film.[85] The LTP bulk achieves an ionic conductivity of 9.3 x 10^{-7} S/cm at RT (6.2x greater than the competing ALD LiPON SSE) and 1.2 x 10^{-5} S/cm at 80 ^oC.

Conclusions and Outlook

This work demonstrates a novel deposition method of a NASICON-like LTP composite thin film by ALD. We elaborated on the complexity of tuning the composition of quaternary material systems through vapor phase surface chemistry. The super-cycling approach allows for a range of stoichiometries which contribute to the structural and electrochemical properties of the film. By tuning the phosphate concentration in the LTP film, the crystallization temperature was reduced from 850 ^{o}C to 650 ^{o}C. In films annealed at 650 ^{o}C for 9 minutes, we report the ionic conductivity of the LTP grains to be 9.3 x 10^{-7} S/cm at RT and 1.7x10^{-5} S/cm at 80 ^{o}C. A secondary phase of anatase TiO_2 is present which contributes an electronic conductivity of 2.5x10^{-7} S/cm at RT. Structural and impedance analysis in this work indicates that there is a continuous electronic pathway due to the high percentage of TiO_2. The secondary phase of TiO_2 in LTP could be useful for applications as a composite electrode (i.e, for lithium ion batteries and pseudocapacitors), where for optimal rate performance the ionic and electronic conductivity should be closely matched.[86]

ALD produces different challenges in materials and process development than other techniques which introduce all the precursors simultaneously (i.e., sol-gel, PLD, sputtering, ball milling etc.). Species in ALD are introduced in a sequential and self-limiting manner; therefore, precursor selection and dosage are crucial in controlling surface reactions that will inevitably dictate the initial state of the as-deposited film. One can take advantage of these attributes to modify the film properties to suit the desired application. This work should be considered a starting point for LTP and NASICON-type titanium phosphate ALD thin films.

This ALD process for mixed metal phosphates is quite adaptable and can be expanded upon by considering the metastable equilibrium states that are normally not accessible with bulk processing methods or in physical vapor deposition. For instance, a mix of TiO_2

and LTP is present in this film due to the incomplete reaction between TTIP and TMP. TMP is known to be very stable and often requires additional activation via plasma-enhanced ALD for reactions with most metalorganic precursors.[44] Furthermore, introducing additional sub-cycles to the LTP process with promising dopants in the NASICON-type structure (e.g., Al^{+3}, Cr^{+3}, Ga^{+3}, Sc^{+3}, Y^{+3}, In^{+3}, or La^{+3}) can lead to even more dramatic gains in Li^+ ion conductivity. Introducing a new dopant can also promote the tunability of properties such as crystallization temperature and film porosity to enable higher compatibility with other relevant device processing in iontronics applications.

Supporting Information

Additional information on the film structures and characterization analysis. [include link to document]

Data Availability

All data will be accessible on the Digital Repository at the University of Maryland

(DRUM): [link will be made available when the data is uploaded].

Corresponding Authors

Keith Gregorczyk: kgregorc@umd.edu

Daniela Fontecha: drfontec@umd.edu

Author Contributions

K.E.G., G.W.R., and D.R.F. developed the plans for the research. D.R.F. developed the ALD process, fabricated devices, and characterized the films. K.E.G., G.W.R., A.C.K., and D.M.S.

provided guidance in the planning of experiments and interpretation of results. A.T.H. prepared the samples for SAED and HRTEM and contributed to the analysis of the sample morphology. J.C. provided guidance in TEM experiments and analysis. D.R.F. wrote the manuscript with input from all authors. All authors approved the final manuscript.

Funding Sources

This work was supported by Murata Integrated Passive Solutions, the U.S. Department of Energy, and the National Science Foundation. Murata supported the evaluation and testing of ALD solid electrolyte materials for application in 3D solid state capacitor structures. Under the Office of Science, Office of Basic Energy Sciences, Grant DE-SC0021070, DOE supported the synthesis of Li-containing titanium phosphates with composition varied through a dopant-supercycle process. Daniela R. Fontecha was supported by the National Science Foundation Graduate Research Fellowship Program under Grant No. DGE 1840340. Any opinions, findings, and conclusions or recommendations expressed in this material are those of the author(s) and do not necessarily reflect the views of the National Science Foundation.

References

(1) Li, Y.; Xiao, S.; Qiu, T.; Lang, X.; Tan, H.; Wang, Y.; Li, Y. Recent Advances on Energy Storage Microdevices: From Materials to Configurations. *Energy Storage Materials*. Elsevier B.V. March 1, 2022, pp 741–767. https://doi.org/10.1016/j.ensm.2021.12.026.

(2) Rubloff, G. W.; Kozen, A. C.; Bok Lee, S. From Nanoscience to Solutions in Electrochemical Energy Storage. *J. Vac. Sci. Technol. A Vacuum, Surfaces, Film.* **2013**, *31* (5), 058503. https://doi.org/10.1116/1.4816262.

(3) Yan, B.; Li, X.; Bai, Z.; Song, X.; Xiong, D.; Zhao, M.; Li, D.; Lu, S. A Review of Atomic Layer Deposition Providing High Performance Lithium Sulfur Batteries. *J. Power Sources* **2017**, *338*, 34–48. https://doi.org/10.1016/j.jpowsour.2016.10.097.

(4) Weimer, A. W. Particle Atomic Layer Deposition. *J Nanopart Res* **2019**, *21* (9).

https://doi.org/10.1007/s11051-018-4442-9.

(5) Lee, M.; Ahmad, W.; Kim, D. W.; Kwon, K. M.; Kwon, H. Y.; Jang, H. Bin; Noh, S. W.; Kim, D. H.; Zaidi, S. J. A.; Park, H.; Lee, H. C.; Abdul Basit, M.; Park, T. J. Powder Coatings via Atomic Layer Deposition for Batteries: A Review. *Chem. Mater.* **2022**, *34* (8), 3539–3587. https://doi.org/10.1021/acs.chemmater.1c02944.

(6) George, S. M.; Ferguson, J. D.; Weimer, A. W. Atomic Layer Controlled Deposition on Particle Surfaces (US Patent 6,613,383 B1), 2003.

(7) George, S. M.; Ferguson, J. D.; Weimer, A. W.; Wank, J. R. Insulating and Functionalizing Fine Metal-Containing Particles with Conformal Ultra-Thin Films. (U.S. Patent 6,713,177). 2004.

(8) Albano, F.; Dahlberg, K.; Anderson, E.; Dhar, S.; Venkatesan, S.; Trevey, J.; King, D. M.; Lichty, P. R. Nano-Engineered Coatings for Anode Active Materials, Cathode Active Materials, and Solid-State Electrolytes and Methods of Making Batteries Containing Nano-Engineered Coatings (US Patent 2016/0351973 A1). **2016**.

(9) Nano, F. High Throughput Apparatus for Manufacturing ALD Coatings (Any Powders) (US Patent No. 9,284,643).

(10) Nano, F. High Throughput Method for Manufacturing ALD Coatings (Any Powder) (US Patent No. 9,546,424).

(11) Sastre, J.; Futscher, M. H.; Pompizi, L.; Aribia, A.; Priebe, A.; Overbeck, J.; Stiefel, M.; Tiwari, A. N.; Romanyuk, Y. E. Blocking Lithium Dendrite Growth in Solid-State Batteries with an Ultrathin Amorphous Li-La-Zr-O Solid Electrolyte. *Commun. Mater.* **2021**, *2* (1). https://doi.org/10.1038/s43246-021-00177-4.

(12) Davis, A. L.; Kazyak, E.; Sakamoto, J.; Dasgupta, N. P.; Garcia-Mendez, R.; Chen, K. H.; Sakamoto, J.; Wood, K. N.; Teeter, G.; Wood, K. N. Electro-Chemo-Mechanical Evolution of Sulfide Solid Electrolyte/Li Metal Interfaces:: Operando Analysis and ALD Interlayer Effects. *J. Mater. Chem. A* **2020**, *8* (13), 6291–6302. https://doi.org/10.1039/c9ta11508k.

(13) Xie, J.; Zhao, J.; Liu, Y.; Wang, H.; Liu, C.; Wu, T.; Hsu, P. C.; Lin, D.; Jin, Y.; Cui, Y. Engineering the Surface of LiCoO2 Electrodes Using Atomic Layer Deposition for Stable High-Voltage Lithium Ion Batteries. *Nano Res.* **2017**, *10* (11), 3754–3764. https://doi.org/10.1007/s12274-017-1588-1.

(14) Pearse, A.; Schmitt, T.; Sahadeo, E.; Stewart, D. M.; Kozen, A.; Gerasopoulos, K.; Talin, A. A.; Lee, S. B.; Rubloff, G. W.; Gregorczyk, K. E. Three-Dimensional Solid-State Lithium-Ion Batteries Fabricated by Conformal Vapor-Phase Chemistry. *ACS Nano* **2018**, *12* (5), 4286–4294. https://doi.org/10.1021/ACSNANO.7B08751.

(15) Ahuja, K.; Sallaz, V.; Nuwayhid, R. B.; Voiron, F.; McCluskey, P.; Rubloff, G. W.; Gregorczyk, K. E. Ultra-Thin on-Chip ALD LiPON Capacitors for High Frequency Application. *J. Power Sources* **2023**, *575* (July 2022), 233056. https://doi.org/10.1016/j.jpowsour.2023.233056.

(16) Fuller, E. J.; Gabaly, F. El; Léonard, F.; Agarwal, S.; Plimpton, S. J.; Jacobs-Gedrim, R. B.; James, C. D.; Marinella, M. J.; Talin, A. A. Li-Ion Synaptic Transistor for Low Power Analog Computing. *Adv. Mater.* **2017**, *29* (4), 1–8. https://doi.org/10.1002/adma.201604310.

(17) Islam, R.; Shi, Y.; de Oliveira Silva, G. V.; Sachdev, M.; Miao, G. X. Volatile and Nonvolatile Programmable Iontronic Memristor with Lithium Imbued TiOx for Neuromorphic Computing Applications. *ACS Nano* **2024**. https://doi.org/10.1021/ACSNANO.4C05137/SUPPL_FILE/NN4C05137_SI_001.PDF.

(18) Patel, K. J.; Bhatt, G. G.; Ray, J. R.; Suryavanshi, P.; Panchal, C. J. All-Inorganic Solid-State Electrochromic Devices: A Review. *J. Solid State Electrochem.* **2017**, *21* (2), 337–347. https://doi.org/10.1007/s10008-016-3408-z.

(19) Wang, S.; Yan, M.; Li, Y.; Vinado, C.; Yang, J. Separating Electronic and Ionic Conductivity in Mix-Conducting Layered Lithium Transition-Metal Oxides. *J. Power Sources* **2018**, *393* (April), 75–82. https://doi.org/10.1016/j.jpowsour.2018.05.005.

(20) Donders, M. E.; Arnoldbik, W. M.; Knoops, H. C. M.; Kessels, W. M. M.; Notten, P. H. L. Atomic Layer Deposition of LiCoO 2 Thin-Film Electrodes for All-Solid-State Li-Ion Micro-Batteries . *J. Electrochem. Soc.* **2013**, *160* (5), A3066–A3071. https://doi.org/10.1149/2.011305jes.

(21) Hallot, M.; Nikitin, V.; Lebedev, O. I.; Retoux, R.; Troadec, D.; De Andrade, V.; Roussel, P.; Lethien, C. 3D LiMn 2 O 4 Thin Film Deposited by ALD: A Road toward High-Capacity Electrode for 3D Li-Ion Microbatteries. **2022**. https://doi.org/10.1002/smll.202107054.

(22) Liu, J.; Banis, M. N.; Sun, Q.; Lushington, A.; Li, R.; Sham, T. K.; Sun, X. Rational Design of Atomic-Layer-Deposited LiFePO4 as a High-Performance Cathode for Lithium-Ion Batteries. *Adv. Mater.* **2014**, *26* (37), 6472–6477. https://doi.org/10.1002/adma.201401805.

(23) Sheil, R.; Butts, D.; Jungjohann, K.; Yoo, J.; Dunn, B.; Chang, J. P. Plasma Enhanced Atomic Layer Deposition of Thin Film Li1+xMn2−xO4 for Realization of All Solid-State 3D Lithium-Ion Microbatteries. *J. Vac. Sci. Technol. A Vacuum, Surfaces, Film.* **2021**, *39* (1). https://doi.org/10.1116/6.0000644.

(24) Stewart, D. M.; Pearse, A. J.; Kim, N. S.; Fuller, E. J.; Talin, A. A.; Gregorczyk, K.; Lee, S. B.; Rubloff, G. W. Tin Oxynitride Anodes by Atomic Layer Deposition for Solid-State Batteries. *Chem. Mater.* **2018**, *30* (8), 2526–2534. https://doi.org/10.1021/acs.chemmater.7b04666.

(25) Meng, X.; Liu, J.; Li, X.; Banis, M. N.; Yang, J.; Li, R.; Sun, X. Atomic Layer Deposited Li4Ti5O12 on Nitrogen-Doped Carbon Nanotubes. *RSC Adv.* **2013**, *3* (20), 7285–7288. https://doi.org/10.1039/c3ra00033h.

(26) Chen, X.; Pomerantseva, E.; Banerjee, P.; Gregorczyk, K.; Ghodssi, R.; Rubloff, G. Ozone-Based Atomic Layer Deposition of Crystalline V2O 5 Films for High Performance Electrochemical Energy Storage. *Chem. Mater.* **2012**, *24* (7), 1255–1261. https://doi.org/10.1021/cm202901z.

(27) Banerjee, P.; Chen, X.; Gregorczyk, K.; Henn-Lecordier, L.; Rubloff, G. W. Mixed Mode, Ionic-Electronic Diode Using Atomic Layer Deposition of V 2O5 and ZnO Films. *J. Mater. Chem.* **2011**, *21* (39), 15391–15397. https://doi.org/10.1039/c1jm12595h.

(28) Niemela, J.-P.; Marin, G.; Karpinen, M. Titanium Dioxide Thin Films by Atomic

Layer: A Review. *Semicond. Sci. Technol.* **2017**, *093005*, 43.

(29) Takada, K.; Tansho, M.; Yanase, I.; Inada, T.; Kajiyama, A.; Kouguchi, M.; Kondo, S.; Watanabe, M. Lithium Ion Conduction in LiTi2(PO4)3. *Solid State Ionics* **2001**, *139* (3–4), 241–247. https://doi.org/10.1016/S0167-2738(01)00688-9.

(30) Nuspl, G.; Takeuchi, T.; Weiß, A.; Kageyama, H.; Yoshizawa, K.; Yamabe, T. Lithium Ion Migration Pathways in LiTi2(PO4)3 and Related Materials. *J. Appl. Phys.* **1999**, *86* (10), 5484–5491. https://doi.org/10.1063/1.371550.

(31) Aono, H.; Sugimoto, E.; Sadaoka, Y.; Imanaka, N.; Adachi, G. Ionic Conductiity and Sinterability of the Lithium Titanium Phosphate System. *Solid State Ionics* **1990**, *41* (2), 38–42.

(32) Aono, H.; Sugimoto, E.; Sadaoka, Y.; Imanaka, N.; Adachi, G. Ionic Conductivity of Solid Electrolytes Based on Li1.3Al0.3Ti1.7(PO4)3. *Russ. J. Appl. Chem.* **1996**, *69* (3), 385–388.

(33) Zhu, J.; Zhao, J.; Xiang, Y.; Lin, M.; Wang, H.; Zheng, B.; He, H.; Wu, Q.; Huang, J. Y.; Yang, Y. Chemomechanical Failure Mechanism Study in NASICON-Type Li1.3Al0.3Ti1.7(PO4)3Solid-State Lithium Batteries. *Chem. Mater.* **2020**, *32* (12), 4998–5008. https://doi.org/10.1021/acs.chemmater.9b05295.

(34) Hartmann, P.; Leichtweiss, T.; Busche, M. R.; Schneider, M.; Reich, M.; Sann, J.; Adelhelm, P.; Janek, J. Degradation of NASICON-Type Materials in Contact with Lithium Metal: Formation of Mixed Conducting Interphases (MCI) on Solid Electrolytes. *J. Phys. Chem. C* **2013**, *117* (41), 21064–21074. https://doi.org/10.1021/jp4051275.

(35) Narváez-Semanate, J. L.; Rodrigues, A. C. M. Microstructure and Ionic Conductivity of Li1 + XAl XTi2-x(PO4)3 NASICON Glass-Ceramics. *Solid State Ionics* **2010**, *181* (25–26), 1197–1204. https://doi.org/10.1016/j.ssi.2010.05.010.

(36) Xiao, W.; Wang, J.; Fan, L.; Zhang, J.; Li, X. Recent Advances in Li1+xAlxTi2−x(PO4)3 Solid-State Electrolyte for Safe Lithium Batteries. *Energy Storage Mater.* **2019**, *19* (August 2018), 379–400. https://doi.org/10.1016/j.ensm.2018.10.012.

(37) Scarpioni, F.; Khalid, S.; Chukwu, R.; Pianta, N.; LaMantia, F.; Ruffo, R. Electrochemical Impedance Spectroscopy for Electrode Process Evaluation: Lithium Titanium Phosphate in Concentrated Aqueous Electrolyte. *ChemElectroChem* **2023**, *10*.

(38) Zhang, Q.; Schierholz, R.; Dzieciol, K.; Yu, S.; Tempel, H.; Kungl, H.; Eichel, R.-A. Microstructural Details of Spindle-like Lithium Titanium Phosphate Revealed in Three Dimensions. *RSC Adv.* **2021**, *11*, 34605–34612. https://doi.org/10.1039/d1ra05754e.

(39) Delmas, C.; Nadiri, A.; Soubeyroux, J. L. The Nasicon-Type Titanium Phosphates Ati2(PO4)3 (A=Li, Na) as Electrode Materials. *Solid State Ionics* **1988**, *28–30* (PART 1), 419–423. https://doi.org/10.1016/S0167-2738(88)80075-4.

(40) Wessells, C.; Mantia, F. La; Deshazer, H.; Huggins, R. A.; Cui, Y. Synthesis and Electrochemical Performance of a Lithium Titanium Phosphate Anode for Aqueous Lithium-Ion Batteries. *J. Electrochem. Soc.* **2011**, *158* (3), 352–355. https://doi.org/10.1149/1.3536619.

(41) Kee, Y.; Dimov, N.; Minami, K.; Okada, S. Electrochimica Acta Orthorhombic Lithium Titanium Phosphate as an Anode Material for Li-Ion Rechargeable Battery. *Electrochim. Acta* **2015**, *174*, 516–520. https://doi.org/10.1016/j.electacta.2015.06.032.

(42) Yu, S.; Tempel, H.; Schierholz, R.; Aslanbas, Ö.; Gao, X.; Mertens, J.; de Haart, L. G. J.; Kungl, H.; Eichel, R. A. LiTi2(PO4)3/C Anode Material with a Spindle-Like Morphology for Batteries with High Rate Capability and Improved Cycle Life. *ChemElectroChem* **2016**, *3* (7), 1157–1169. https://doi.org/10.1002/celc.201600125.

(43) Wang, G. X.; Bradhurst, D. H.; Dou, S. X.; Liu, H. K. LiTi2(PO4)3 with NASICON-Type Structure as Lithium-Storage Materials. *J. Power Sources* **2003**, *124* (1), 231–236. https://doi.org/10.1016/S0378-7753(03)00609-8.

(44) Aatiq, A.; Ménétrier, M.; Croguennec, L.; Suard, E.; Delmas, C. On the Structure of Li3Ti2(Po4)3. *J. Mater. Chem.* **2002**, *12* (10), 2971–2978. https://doi.org/10.1039/b203652p.

(45) He, Y.; Zhang, Z.; Feng, G.; Li, H. Two-Dimensional LiTi2(PO4)3 Flakes for Enhanced Lithium Ions Battery Anode. *Heliyon* **2024**, *10* (1), e23396. https://doi.org/10.1016/j.heliyon.2023.e23396.

(46) Mackus, A. J. M.; Schneider, J. R.; Macisaac, C.; Baker, J. G.; Bent, S. F. Synthesis of Doped, Ternary, and Quaternary Materials by Atomic Layer Deposition: A Review. *Chem. Mater.* **2019**, *31* (4), 1142–1183. https://doi.org/10.1021/acs.chemmater.8b02878.

(47) Banerjee, P.; Lee, W. J.; Bae, K. R.; Lee, S. B.; Rubloff, G. W. Structural, Electrical, and Optical Properties of Atomic Layer Deposition Al-Doped ZnO Films. In *Journal of Applied Physics*; 2010; Vol. 108. https://doi.org/10.1063/1.3466987.

(48) Militzer, C.; Buchsbaum, J.; Dzhagan, V.; Zahn, D. R. T.; Wulff, H.; Helm, C. A.; Goedel, W. A. Atomic Layer Deposition of Titanium Phosphate from Titanium Tetrachloride and Triethyl Phosphate onto Carbon Fibers. *Adv. Mater. Interfaces* **2018**, *5* (16), 1–11. https://doi.org/10.1002/admi.201800423.

(49) Hämäläinen, J.; Holopainen, J.; Munnik, F.; Heikkilä, M.; Ritala, M.; Leskelä, M. Atomic Layer Deposition of Aluminum and Titanium Phosphates. *J. Phys. Chem. C* **2012**, *116* (9), 5920–5925. https://doi.org/10.1021/jp205222g.

(50) Wiedmann, M. K.; Jackson, D. H. K.; Pagan-Torres, Y. J.; Cho, E.; Dumesic, J. A.; Kuech, T. F. Atomic Layer Deposition of Titanium Phosphate on Silica Nanoparticles. *J. Vac. Sci. Technol. A Vacuum, Surfaces, Film.* **2012**, *30* (1). https://doi.org/10.1116/1.3664097.

(51) Getz, M. N.; Hansen, P. A.; Fjellvåg, H.; Nilsen, O. Luminescent Properties of Europium Titanium Phosphate Thin Films Deposited by Atomic Layer Deposition. *RSC Adv.* **2017**, *7* (13), 8051–8059. https://doi.org/10.1039/c6ra27644j.

(52) Dill, P.; Ren, X.; Hintersatz, H.; Franz, M.; Dentel, D.; Tegenkamp, C.; Ebert, S. Atomic Layer Deposition of Titanium Phosphate onto Reinforcing Fibers Using Titanium Tetrachloride, Water, and Tris(Trimethylsilyl) Phosphate as Precursors. *J. Vac. Sci. Technol. A* **2022**, *40* (2), 022403. https://doi.org/10.1116/6.0001514.

(53) Henderick, L.; Hamed, H.; Mattelaer, F.; Minjauw, M.; Nisula, M.; Meersschaut, J.;

Dendooven, J.; Safari, M.; Vereecken, P.; Detavernier, C. Plasma Enhanced Atomic Layer Deposition of a (Nitrogen Doped) Ti Phosphate Coating for Improved Energy Storage in Li-Ion Batteries. *J. Power Sources* **2021**, *497* (February), 229866. https://doi.org/10.1016/j.jpowsour.2021.229866.

(54) Dobbelaere, T.; Mattelaer, F.; Roy, A. K.; Vereecken, P.; Detavernier, C. Plasma-Enhanced Atomic Layer Deposition of Titanium Phosphate as an Electrode for Lithium-Ion Batteries. *J. Mater. Chem. A* **2017**, *5* (1), 330–338. https://doi.org/10.1039/c6ta04179e.

(55) Wang, B.; Liu, J.; Sun, Q.; Xiao, B.; Li, R.; Sham, T. Titanium Dioxide / Lithium Phosphate Nanocomposite Derived from Atomic Layer Deposition as a High-Performance Anode for Lithium Ion Batteries. **2016**. https://doi.org/10.1002/admi.201600369.

(56) Henderick, L.; Hamed, H.; Mattelaer, F.; Minjauw, M.; Nisula, M.; Meersschaut, J.; Dendooven, J.; Safari, M.; Vereecken, P.; Detavernier, C. Plasma Enhanced Atomic Layer Deposition of a (Nitrogen Doped) Ti Phosphate Coating for Improved Energy Storage in Li-Ion Batteries. *J. Power Sources* **2021**, *497* (February). https://doi.org/10.1016/j.jpowsour.2021.229866.

(57) Kozen, A. C.; Pearse, A. J.; Lin, C. F.; Schroeder, M. A.; Noked, M.; Lee, S. B.; Rubloff, G. W. Atomic Layer Deposition and in Situ Characterization of Ultraclean Lithium Oxide and Lithium Hydroxide. *J. Phys. Chem. C* **2014**, *118* (48), 27749–27753. https://doi.org/10.1021/jp509298r.

(58) Subramanian, M. A.; Subramanian, R.; Clearfield, A. Lithium Ion Conductors in the System AB(IV)2(PO4)3 (B=Ti,Zr and Hf). *Solid State Ionics* **1986**, *18* & *19*, 562–569.

(59) Balachandran, U.; Eror, N. G. Raman Spectra of Titanium Dioxide. *J. Solid State Chem.* **1982**, *42* (3), 276–282. https://doi.org/10.1016/0022-4596(82)90006-8.

(60) Tompsett, G. A.; Bowmaker, G. A.; Cooney, R. P.; Metson, J. B.; Rodgers, K. A.; Seakins, J. M. The Raman Spectrum of Brookite, TiO2 (Pbca, Z = 8). *J. Raman Spectrosc.* **1995**, *26* (1), 57–62. https://doi.org/10.1002/jrs.1250260110.

(61) Pérez-Estébanez, M.; Isasi-Marín, J.; Díaz-Guerra, C.; Rivera-Calzada, A.; León, C.; Santamaría, J. Influence of Chromium Content on the Optical and Electrical Properties of Li1 + XCrxTi2 - X(PO4)3. *Solid State Ionics* **2013**, *241*, 36–45. https://doi.org/10.1016/j.ssi.2013.04.001.

(62) Popović, L.; Manoun, B.; De Waal, D.; Nieuwoudt, M. K.; Comins, J. D. Raman Spectroscopic Study of Phase Transitions in Li3PO4. *J. Raman Spectrosc.* **2003**, *34* (1), 77–83. https://doi.org/10.1002/jrs.954.

(63) Petersen, H.; Stegmann, N.; Fischer, M.; Zibrowius, B.; Radev, I.; Philippi, W.; Schmidt, W.; Weidenthaler, C. Crystal Structures of Two Titanium Phosphate-Based Proton Conductors: Ab Initio Structure Solution and Materials Properties. *Inorg. Chem.* **2022**, *61* (5), 2379–2390. https://doi.org/10.1021/acs.inorgchem.1c02613.

(64) Laskova, B.; Frank, O.; Zukalova, M.; Bousa, M.; Dracinsky, M.; Kavan, L. Lithium Insertion into Titanium Dioxide (Anatase): A Raman Study with 16/18O and 6/7Li Isotope Labeling. *Chem. Mater.* **2013**, *25* (18), 3710–3717. https://doi.org/10.1021/cm402056j.

(65) Bamberger, C. E.; Macdougall, C. S.; Begun, G. M.; Hatmaker, T. L. Synthesis of Solid Phosphate Compounds of Ti (Lll) and Ti (IV). **1991**, *41*, 837–841.

(66) Bamberger, C. E.; Begun, G. M.; Cavin, O. B. Synthesis and Characterization of Sodium-Titanium Phosphates, Na4(TiO)(PO4)2, Na(TiO)PO4, and NaTi2(PO4)3. *J. Solid State Chem.* **1988**, *73* (2), 317–324. https://doi.org/10.1016/0022-4596(88)90115-6.

(67) Schiffmann, N.; Bucharsky, E. C.; Schell, K. G.; Fritsch, C. A.; Knapp, M.; Hoffmann, M. J. Upscaling of LATP Synthesis: Stoichiometric Screening of Phase Purity and Microstructure to Ionic Conductivity Maps. *Ionics (Kiel).* **2021**, *27* (5), 2017–2025. https://doi.org/10.1007/s11581-021-03961-x.

(68) Wu, X. M.; Chen, S.; Mai, F. R.; Zhao, J. H.; He, Z. Q. Influence of the Annealing Technique on the Properties of Li Ion-Conductive Li1.3Al0.3Ti1.7(PO4)3 Films. *Ionics (Kiel).* **2013**, *19* (4), 589–593. https://doi.org/10.1007/s11581-012-0788-7.

(69) Aarik, J.; Aidla, A.; Uustare, T.; Ritala, M.; Leskela, M. *Titanium Isopropoxide as a Precursor for Atomic Layer Deposition: Characterization of Titanium Dioxide Growth Process*; 2000; Vol. 161.

(70) Pearse, A. J.; Schmitt, T. E.; Fuller, E. J.; El-Gabaly, F.; Lin, C. F.; Gerasopoulos, K.; Kozen, A. C.; Talin, A. A.; Rubloff, G.; Gregorczyk, K. E. Nanoscale Solid State Batteries Enabled by Thermal Atomic Layer Deposition of a Lithium Polyphosphazene Solid State Electrolyte. *Chem. Mater.* **2017**, *29* (8), 3740–3753. https://doi.org/10.1021/acs.chemmater.7b00805.

(71) Grey, L. H.; Nie, H. Y.; Biesinger, M. C. Defining the Nature of Adventitious Carbon and Improving Its Merit as a Charge Correction Reference for XPS. *Appl. Surf. Sci.* **2024**, *653* (December 2023), 159319. https://doi.org/10.1016/j.apsusc.2024.159319.

(72) Kozen, A. C.; Pearse, A. J.; Lin, C. F.; Noked, M.; Rubloff, G. W. Atomic Layer Deposition of the Solid Electrolyte LiPON. *Chem. Mater.* **2015**, *27* (15), 5324–5331. https://doi.org/10.1021/acs.chemmater.5b01654.

(73) Wang, B.; Liu, J.; Sun, Q.; Li, R.; Sham, T.-K.; Sun, X. Atomic Layer Deposition of Lithium Phosphates as Solid-State Electrolytes for All-Solid-State Microbatteries. *2Nanotechnology* **2014**, *25* (504007).

(74) Zhao, Y.; Chen, P.; Zhang, B.; Su, D. S.; Zhang, S.; Tian, L.; Lu, J.; Li, Z.; Cao, X.; Wang, B.; Wei, M.; Evans, D. G.; Duan, X. Highly Dispersed TiO6 Units in a Layered Double Hydroxide for Water Splitting. *Chem. - A Eur. J.* **2012**, *18* (38), 11949–11958. https://doi.org/10.1002/chem.201201065.

(75) Zhang, Q.; Zhang, X.; Zhang, Y.; Shen, Q. Influence of Lithium Phosphate on the Structural and Lithium-Ion Conducting Properties of Lithium Aluminum Titanium Phosphate Pellets. *Ionics (Kiel).* **2021**, *27* (6), 2473–2481. https://doi.org/10.1007/s11581-021-04011-2.

(76) Wagemaker, M.; Van de Krol, R.; Kentgens, A. P. M.; Van Well, A. A.; Mulder, F. M. Two Phase Morphology Limits Lithium Diffusion in TiO2 (Anatase): A 7Li MAS NMR Study. *J. Am. Chem. Soc.* **2001**, *123* (46), 11454–11461. https://doi.org/10.1021/ja0161148.

(77) Morimoto, H.; Ito, D.; Ogata, Y.; Suzuki, T.; Sakamaki, K.; Tsuji, T.; Hirukawa, M.;

Matsumoto, A.; Tobishima, S. I. Charge/Discharge Behavior of Triclinic Litiopo4 Anode Materials for Lithium Secondary Batteries. *Electrochemistry* **2016**, *84* (11), 878–881. https://doi.org/10.5796/electrochemistry.84.878.

(78) Hupfer, T.; Bucharsky, E. C.; Schell, K. G.; Hoffmann, M. J. Influence of the Secondary Phase LiTiOPO4 on the Properties of Li1 + XAlxTi2 − x(PO4)3 (x = 0; 0.3). *Solid State Ionics* **2017**, *302*, 49–53. https://doi.org/10.1016/j.ssi.2016.10.008.

(79) Huggins, R. A. Simple Method to Determine Electronic Conductivity in Mixed A Review and Ionic Components of the Conductors. *300 Ionics* **2002**, *8*.

(80) Pomoni, K.; Sofianou, M. V.; Georgakopoulos, T.; Boukos, N.; Trapalis, C. Electrical Conductivity Studies of Anatase TiO2 with Dominant Highly Reactive {0 0 1} Facets. *J. Alloys Compd.* **2013**, *548*, 194–200. https://doi.org/10.1016/j.jallcom.2012.08.136.

(81) Huang, S. Y.; Kavan, L.; Exnar, I.; Gratszel, M. Rocking Chair Lithium Battery Based on Nanocrystalline TiO (Anatase). *J. Electrochem. Soc* **1995**, *142* (9), 142–144.

(82) Kosova, N.; Devyatkina, E.; Osintsev, D. Dispersed Materials for Rechargeable Lithium Batteries: Reactive and Non-Reactive Grinding. *J. Mater. Sci.* **2004**, *39* (16–17), 5031–5036. https://doi.org/10.1023/B:JMSC.0000039181.03644.b0.

(83) Werbrouck, A.; Mattelaer, F.; Dhara, A.; Nisula, M.; Minjauw, M.; Munnik, F.; Dendooven, J.; Detavernier, C. Surface Reactions between LiHMDS, TMA and TMP Leading to Deposition of Amorphous Lithium Phosphate. *J. Mater. Chem. A* **2022**. https://doi.org/10.1039/D1TA09500E.

(84) Wang, C.; Xu, B. Bin; Zhang, X.; Sun, W.; Chen, J.; Pan, H.; Yan, M.; Jiang, Y. Ion Hopping : Design Principles for Strategies to Improve Ionic Conductivity for Inorganic Solid Electrolytes. **2022**, *2107064*, 1–17. https://doi.org/10.1002/smll.202107064.

(85) Siller, V.; Morata, A.; Nunez Eroles, M.; Arenal, P.; Gonzales-Rosillo, J. C.; Lopez del Amo, J. Mi.; Tarancon, A. High Performance LATP Thin Film Electrolytes for All-Solid-State Microbattery Applications. *J. Mater. Chem. A* **2021**, *9* (17760).

(86) Minnmann, P.; Quillman, L.; Burkhardt, S.; Richter, F. H.; Janek, J. Quantifying the Impact of Charge Transport Bottlenecks in Composite Cathodes of All-Solid-State Batteries. *J. Electrochem. Soc.* **2021**, *168* (4), 040537. https://doi.org/10.1149/1945-7111/abf8d7.